Astronomy & Astrophysics manuscript no. at25_emission_v3
November 23, 2021

Letter to the Editor

The GAPS Programme at TNG

XXXIII. HARPS-N detects multiple atomic species in emission from the dayside of KELT-20b⋆

F. Borsa[1], A. S. Bonomo[2], M. Brogi[3,2,4], P. Giacobbe[2], L. Pino[5], L. Fossati[6], A. F. Lanza[7], V. Nascimbeni[8], A. Sozzetti[2], S. Benatti[9], K. Biazzo[10], A. Bignamini[11], W. Boschin[12,13,14], R. Claudi[8], R. Cosentino[12], E. Covino[15], S. Desidera[8], A. F. M. Fiorenzano[12], G. Guilluy[2], A. Harutyunyan[12], A. Maggio[9], J. Maldonado[9], L. Mancini[16,17,2], G. Micela[9], E. Molinari[18], M. Molinaro[11], I. Pagano[7], M. Pedani[12], G. Piotto[19], E. Poretti[1,12], G. Scandariato[7], H. Stoev[12]

[1] INAF – Osservatorio Astronomico di Brera, Via E. Bianchi 46, 23807 Merate (LC), Italy
[2] INAF – Osservatorio Astrofisico di Torino, Via Osservatorio 20, 10025, Pino Torinese, Italy
[3] Department of Physics, University of Warwick, Coventry CV4 7AL, UK
[4] Centre for Exoplanets and Habitability, University of Warwick, Gibbet Hill Road, Coventry CV4 7AL, UK
[5] INAF – Osservatorio Astrofisico di Arcetri, Largo E. Fermi 5, 50125 Firenze, Italy
[6] Space Research Institute, Austrian Academy of Sciences, Schmiedlstrasse 6, A-8042 Graz, Austria
[7] INAF – Osservatorio Astrofisico di Catania, Via S.Sofia 78, 95123, Catania, Italy
[8] INAF – Osservatorio Astronomico di Padova, Vicolo dell'Osservatorio 5, 35122, Padova, Italy
[9] INAF – Osservatorio Astronomico di Palermo, Piazza del Parlamento, 1, 90134, Palermo, Italy
[10] INAF – Osservatorio Astronomico di Roma, via Frascati 33, I00040, Monte Porzio Catone (RM), Italy
[11] INAF – Osservatorio Astronomico di Trieste, via Tiepolo 11, 34143 Trieste, Italy
[12] Fundación Galileo Galilei - INAF, Rambla José Ana Fernandez Pérez 7, 38712 Breña Baja, TF - Spain
[13] Instituto de Astrofísica de Canarias (IAC), C/Vía Láctea s/n, 38205 La Laguna, TF - Spain
[14] Departamento de Astrofísica, Universidad de La Laguna (ULL), 38206 La Laguna, TF - Spain
[15] INAF – Osservatorio Astronomico di Capodimonte, Salita Moiariello 16, 80131, Napoli, Italy
[16] Department of Physics, University of Rome Tor Vergata, Via della Ricerca Scientifica 1, I-00133 Rome, Italy
[17] Max Planck Institute for Astronomy, Königstuhl 17, D-69117, Heidelberg, Germany
[18] INAF – Osservatorio di Cagliari, via della Scienza 5, I-09047 Selargius, CA, Italy
[19] Dip. di Fisica e Astronomia Galileo Galilei – Università di Padova, Vicolo dell'Osservatorio 2, 35122, Padova, Italy

Received ; accepted

ABSTRACT

The detection of lines in emission in planetary atmospheres is direct evidence of temperature inversion. We confirm the trend of ultra-hot Jupiters orbiting A-type stars showing temperature inversions on their daysides, by adding KELT-20b to the list of planets with detected metals emission lines. We first detect the planetary emission by using the G2 stellar mask of the HARPS-N pipeline, which is mainly composed of neutral iron lines, as a template. Then we create models of planetary emission of different species assuming an inverted temperature-pressure atmospheric profile. By using the cross-correlation technique, we detect Fe I, Fe II and Cr I. The latter is detected for the first time in emission in the atmosphere of an exoplanet. Contrary to Fe I, Fe II and Cr I are detected only after the occultation and not before, hinting for different atmospheric properties in view on the pre- and post- occultation orbital phases.

Key words. planetary systems – techniques: spectroscopic – planets and satellites: atmospheres – stars:individual:KELT-20

1. Introduction

Ultra-hot Jupiters (UHJs) are highly irradiated gas giant planets with equilibrium temperatures exceeding 2000 K and hosting atmospheres presenting substantial H_2 dissociation and H^- opacity (e.g., Arcangeli et al. 2018; Parmentier et al. 2018; Bell & Cowan 2018). They show different atmospheric properties from the classic hot Jupiters. In particular, one key characteristic is the atmospheric thermal inversion, which appears to happen when the equilibrium temperature reaches ∼1700 K, with observational evidence for a transition between the two regimes (Baxter et al. 2020). Fossati et al. (2021) showed that non-LTE effects play a significant role in determining the shape of the temperature inversion. While previous studies predicted the temperature inversion to be caused mainly by TiO and VO (e.g. Hubeny et al. 2003; Fortney et al. 2008), more recent works showed that also the presence of metals alone (coupled with dissociation in the near-infrared) can cause atmospheric inversions (e.g. Lothringer

Send offprint requests to: F. Borsa
e-mail: francesco.borsa@inaf.it

⋆ Based on observations made with the Italian Telescopio Nazionale Galileo (TNG) operated on the island of La Palma by the Fundacion Galileo Galilei of the INAF at the Spanish Observatorio Roque de los Muchachos of the IAC in the frame of the program Global Architecture of the Planetary Systems (GAPS).

et al. 2018; Lothringer & Barman 2019). Lothringer & Barman (2019) suggest that UHJ can have a temperature inversion originating from atomic absorptions depending on the stellar spectral type. This presence of metals has been observationally confirmed with high-resolution spectroscopy.

High-resolution spectroscopy allows us to distinguish the planetary spectrum from the stellar one, thanks to the fact that it can resolve the Doppler shift of the planetary lines caused by the orbital motion in the star-planet system. Moreover, it gives the possibility to resolve individual lines, ensuring the unambiguous detection of atomic and molecular species. High-resolution emission spectroscopy can thus help in determining which are the species that cause the inversion in the atmospheric temperature-pressure (T-P) profiles of UHJs. After the first detection of neutral iron emission from the day-side of an exoplanet for the UHJ KELT-9b (Pino et al. 2020), later confirmed by Kasper et al. (2021), neutral iron emission at high resolution was discovered also for WASP-33b (Nugroho et al. 2020) and WASP-189b (Yan et al. 2020), two other UHJ orbiting A-type stars.

KELT-20b (Lund et al. 2017), also known as MASCARA-2b (Talens et al. 2018), is an ultra-hot Jupiter ($T_{\rm eq}$ ~2200 K) orbiting a fast rotating ($v \sin i$~116 km s^{-1}) A2-type star in ~3.5 days. Its atmosphere is the subject of many investigations, with high-resolution transmission spectroscopy leading to the detection of different species like Na, H, Mg, Fe I, Fe II, Ca II, Cr and possibly FeH (Casasayas-Barris et al. 2018, 2019; Stangret et al. 2020; Nugroho et al. 2020; Hoeijmakers et al. 2020; Kesseli et al. 2020). The Fe I features have been further used to detect the atmospheric Rossiter-McLaughlin effect (Rainer et al. 2021) and to bring evidence of probable atmospheric variability (Nugroho et al. 2020; Rainer et al. 2021).

In this work we present the high-resolution detection of multiple-species emission from the dayside of KELT-20b, probing a temperature inversion in its atmosphere. In Sect. 2 we present our dataset, and in Sect. 3 the detection of emission from the planet. We then search for emission from different atomic species in Sect. 4, and conclude with a discussion and final remarks in Sect. 5.

2. Data sample

In the framework of the GAPS programme (Borsa et al. 2019; Guilluy et al. 2020; Giacobbe et al. 2021), we observed KELT-20 with the HARPS-N and GIANO-B high-resolution spectrographs, mounted at the Telescopio Nazionale Galileo. We used the GIARPS configuration (Claudi et al. 2017), which allows us to simultaneously use the two spectrographs, obtaining high-resolution spectra in the wavelength range ~390-690 nm and ~940-2420 nm. In this work, we analyse only the HARPS-N spectra. Considering the transit centered at phase 0, with our observations we covered the orbital phases 0.40-0.44 and 0.53-0.59 of KELT-20b. Observations were taken with exposures of 600 sec. While fiber A of the spectrograph was centered on the target, fiber B was monitoring the sky simultaneously. During both nights weather conditions suffered by some calima. A log of the observations is reported in Table 1.

Table 1. KELT-20b HARPS-N observations log.

Night #	Night[1]	Phase	N_{obs}	Airmass	S/N_{ave}
1	11 Oct 2020	0.53-0.59	30	1.0-2.5	165
2	14 Oct 2020	0.40-0.44	25	1.1-2.0	200

[1]Start of night civil date.

3. Planetary emission detection

We first tried to see if the planetary emission was visible directly from the stellar cross-correlation functions (CCFs). We started our analysis from the CCFs extracted by version 3.7 of the HARPS-N Data Reduction Software (DRS) pipeline (Cosentino et al. 2014), using the YABI interface with custom parameters (e.g., Borsa et al. 2015). In particular, we used a G2 stellar mask and enlarged the CCF width to the range [-300:300] km s^{-1}. This was done to take into account the large $v \sin i$ of the star and to sample the velocity range of the possible planetary signal, which is expected to appear dozens of km s^{-1} away from the stellar one. The stellar mask used to compute the CCF is mainly composed by Fe I lines (which represent most of the weighted spectroscopic information of a stellar mask, Ehrenreich et al. 2020), so it is a good indicator of neutral iron.

We analysed each of the two nights of observations (Table 1) independently. We first put the CCFs in the stellar rest frame using the Keplerian orbital solution calculated with the parameters of Table A.1. The CCFs suffered from an evident slope, due to the imperfect color correction caused by the spectral type of the star, which does not have a proper color correction template. We thus normalised the CCFs by dividing for a linear fit performed excluding the range [-140:140] km s^{-1} (i.e. we fit only the continuum). Then we created a master CCF (CCF_{master}) by doing a median of all the CCFs, and divided all the CCFs for this CCF_{master}. This normalisation allowed us to cancel the stellar spectrum but not the planetary one, which moves on different pixels during the observations, unlike the stellar one which is almost static. The median approach has been already successfully used in other works involving planetary emission (Pino et al. 2020) or looking for planetary albedo reflection (Scandariato et al. 2020). At this point of the analysis, in the obtained CCF residuals (CCF_{res}) the presence of the planetary signal was already slightly noticeable in both nights (Fig. 1, left panels).

For a range of K_p values from 0 to 300 km s^{-1}, in steps of 1 km s^{-1}, we averaged the CCF_{res} after shifting them in the planetary rest frame, which was done by subtracting the planetary radial velocity computed for each exposure as $v_p = K_p \times \sin 2\pi\phi$, with ϕ the orbital phase. We thus created the K_p-ΔV_{sys} maps, that we used to check the presence of a significant signal close to the expected planetary K_p (Fig. 1, central panels). We then looked at the signal at the expected K_p (175 km s^{-1}), and performed a Gaussian fit to measure its amplitude (Fig. 1, right panels).

There is a significant detection of planetary emission for both nights, with signal-to-noise (S/N) levels of 3.2 and 4.0 for night 1 and night 2, respectively. The S/N of the detections is calculated with respect to the noise level of the continuum (~27-28 ppm on both nights), which was evaluated by calculating the standard deviation of the K_p-ΔV_{sys} maps far from where any stellar or planetary signal is expected. The planetary signal is detected in emission, which is an unambiguous sign of thermal inversion in its atmosphere (Pino et al. 2020). The results of the Gaussian fits are shown in Table 2, expressed as the ratio between planetary and stellar flux. The amplitudes of the planetary signal at the theoretical K_p are consistent for both nights, but there is difference in their FWHMs. We note that pre- and post-occultation orbital phases show different regions of the planetary atmosphere, and any difference because of non-identical temperature, chem-

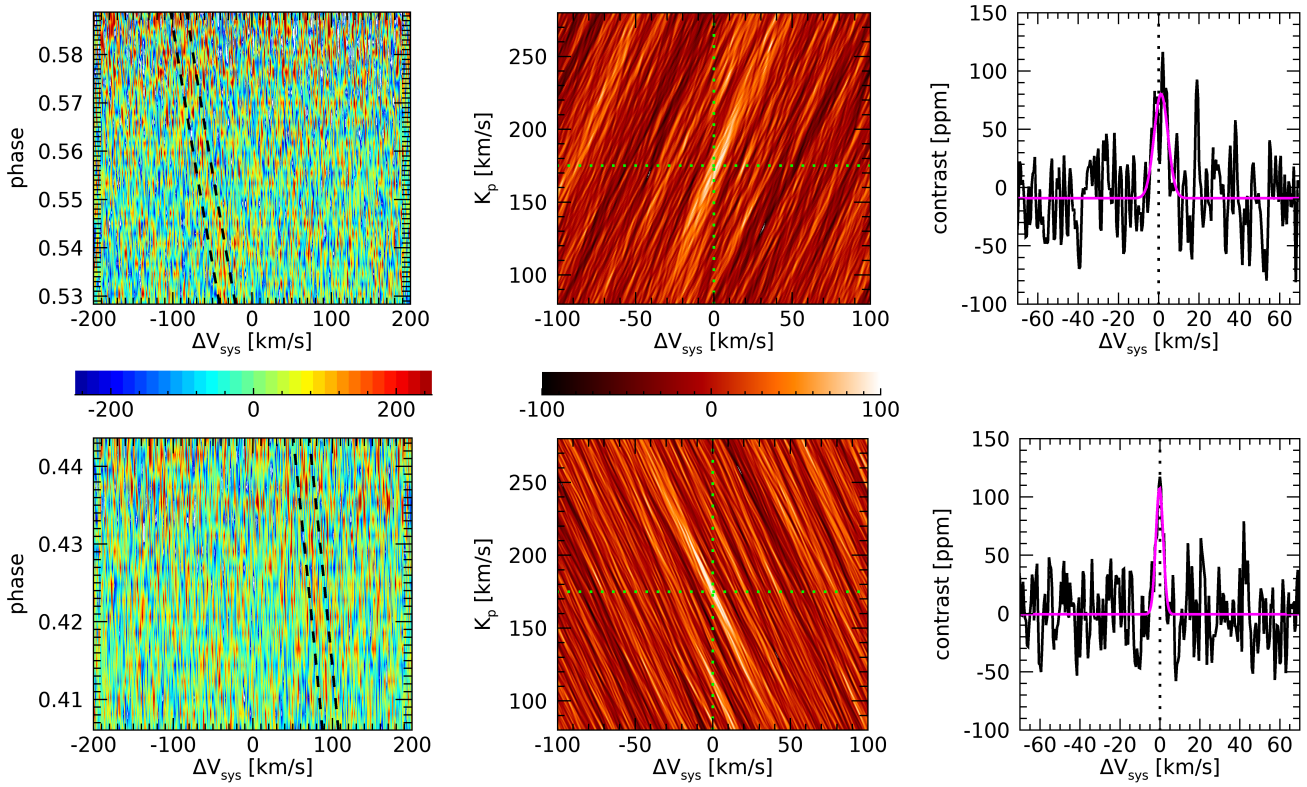

Fig. 1. The first row refers to night 1 and the second row to night 2. *(Left panels)*: 2D tomography of the CCF residuals maps. The dashed lines bracket the expected planetary signal position. *(Central panels)*: K_p-ΔV_{sys} maps. The green dotted lines mark the theoretical planetary position. *(Right panels)*: Planetary emission signal averaged at the theoretical K_p. The magenta line represents the Gaussian fit to the data.

Table 2. KELT-20b emission detections with the stellar G2 mask as a template.

Night	contrast [ppm]	center [km s^{-1}]	FWHM [km s^{-1}]
1	89±10	1.1± 0.5	8.1±1.1
2	108±12	-0.2± 0.2	4.3 ±0.7

ical composition and abundances is indeed possible. By using the theoretical K_p for two different nights and different orbital phases, here we assumed a circular and perfect orbital solution and that there are no detectable atmospheric dynamics in the planetary atmosphere. This latter point, in particular, has been questioned by recent results on this planet (Nugroho et al. 2020; Rainer et al. 2021). Comparing in detail the results of different nights taken at different orbital phases to constrain the three dimensional characteristics of a planetary atmosphere requires a careful and well defined analysis framework. Such a framework is out of the scope of this manuscript and will be the subject of another work (Pino et al. in prep.).

We then combined together the K_p-ΔV_{sys} maps of the two nights (Fig. 2). We fitted the combined map with a 2D Gaussian, obtaining values of K_p=173±9 km s^{-1}and ΔV_{sys}=0.6±3.6 km s^{-1}.

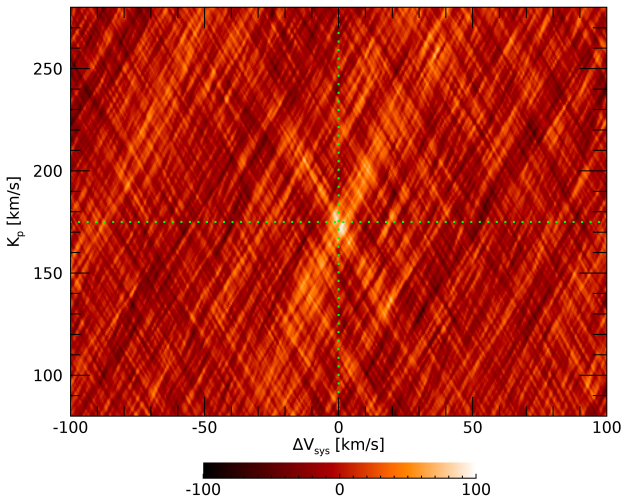

Fig. 2. K_p-ΔV_{sys} map of the two nights combined. The green dotted lines mark the expected planetary position at K_p=175 km s^{-1}. The colour scale is in ppm.

4. Searching for atomic species

The detection of emission from the planet using the stellar G2 template proved the presence of mainly neutral iron emission (Sect. 3), as the neutral iron lines are the main component of the G2 mask. We then decided to see if we could detect emission

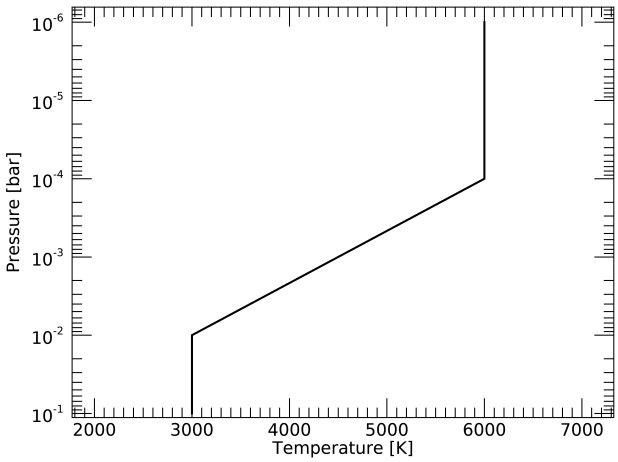

Fig. 3. T-P profile assumed for the dayside of KELT-20b in this work.

from single atomic species. We looked first at Fe I, to confirm that this is the main source of the detection with the stellar mask. Then we looked also for Fe II, Ti I and Cr I, which are among the other principal components of the stellar mask (e.g., Ehrenreich et al. 2020).

Emission model spectra for the planetary atmosphere were generated by using `petitRADTRANS` (Mollière et al. 2019), assuming solar metallicity and equilibrium chemistry. Following Yan et al. (2020), we assumed a two-points T-P profile (Fig. 3). The temperatures in the atmosphere below the higher pressure point and beyond the lower pressure point are considered isothermal, while the slope between the two points is defined by a gradient

$$T_{\rm slope} = \frac{T_2 - T_1}{\log_{10} P_2 - \log_{10} P_1} \quad (1)$$

with the temperature changing linearly with $\log_{10} P$. In this work, we assumed T_1=3000 K, T_2=6000 K, P_1=0.01 bar, P_2=0.0002 bar. This assumption is justified by the fact that for other UHJs atmospheric temperatures have been measured to be much higher than the expected equilibrium temperature (e.g., Yan et al. 2020; Fossati et al. 2020). We note that with higher S/N data, the T-P profile could eventually be retrieved from the data in the same way as in Yan et al. (2020), a method that does not reach convergence on our dataset.

The generated model spectra were then divided for a stellar blackbody spectrum with $T_{\rm eff}$=8980 K (Table A.1) to have the model in units F_p/F_s, convolved with the instrumental profile (assuming a resolving power of 115,000) and continuum normalised. When using a stellar blackbody spectrum we ignore the dependence on the stellar lines. The Fe I, Ti I and Cr I models present many emission lines, thus making them sensitive to the cross-correlation method (Fig. B.1). This is not the case for the Fe II model, which however shows lines much more prominent.

After normalising the stellar spectra, we corrected for tellurics by exploiting the relation between their depth and airmass (e.g., Snellen et al. 2008; Vidal-Madjar et al. 2010). Then we created a master stellar spectrum by shifting the spectra in the stellar rest frame and taking a median spectrum. The orbital velocity of the planet coupled with the instrumental resolution ensures that the planetary signal is removed from this master spectrum (e.g., Scandariato et al. 2020). All the spectra were then normalised for this master stellar spectrum, and the cross-correlation between the data and the model was done on these residual spectra. The cross-correlation was performed as in Borsa et al. (2021), normalising the model to unity and thus preserving the flux information (e.g., Hoeijmakers et al. 2019).

In our analysis, we imposed all the model lines with contrast less than 1% of the maximum one in our wavelength range to be at zero (e.g., Hoeijmakers et al. 2019). We selected a step of 1 $\rm km\,s^{-1}$ and a velocity range [-300,300] $\rm km\,s^{-1}$. The spectra were divided into segments of 200 Å, then the cross-correlation was performed for each segment covering the range 3900-6500 Å. We performed a 5σ-clipping to eliminate outliers and masked the wavelength range 5240-5280 Å (i.e., the most affected by telluric contamination). Then for each exposure, we applied a weighted average of the cross-correlations of the single segments, where the weights applied to each segment were the square of the inverse of its standard deviation and the depths of the lines in the model.

For a range of K_p values from 0 to 300 $\rm km\,s^{-1}$, in steps of 1 $\rm km\,s^{-1}$, we averaged all the cross-correlation functions after shifting them in the planetary restframe. This was done by subtracting the planetary radial velocity calculated for each spectrum as $v_p = K_p \times \sin 2\pi\phi$, with ϕ the orbital phase. We thus created the K_p versus ΔV_{sys} maps, to check that the signal is found close to the planet radial-velocity semi-amplitude and stellar systemic velocity, as is expected if the signal is of planetary origin. We then evaluated the noise by calculating the standard deviation of the K_p versus ΔV_{sys} maps far from where any stellar or planetary signal is expected. The S/N of the detections (Table 3) was calculated by dividing the best K_p cross-correlation function by the noise, and by fitting a Gaussian function to the result (see Fig. 4 for the detections of night 1).

The results indicate the detection of Fe I in both nights, with S/N of 5.3 and 7.0, respectively. On the first night, we also detect Fe II with S/N=4.1 and Cr I with S/N=3.5. These two elements are not detected in night 2, while the level of noise is comparable to that of night 1. The results of the cross-correlations in individual nights and combining the two nights are reported in Table 3. We note that when combining the two nights, the S/N of the detections of Fe II and Cr I remains almost the same. This gives us further confidence in the reliability of the planetary signal, as also without detection when adding the second night this does not bring a strong destructive interference.

To assess the significance of our detections that we got only in one night, we performed also other statistical tests on this night only. The first one is performed by comparing the in-trail versus out-of-trail samples of the cross-correlation functions and performing a Welch t-test (e.g., Birkby et al. 2017; Nugroho et al. 2017; Brogi et al. 2018; Guilluy et al. 2019). To avoid oversampling, we resampled the cross-correlation functions to 1.5 $\rm km\,s^{-1}$, which is about twice the average pixel size of the instrument (~0.8 $\rm km\,s^{-1}$, Cosentino et al. 2014) and close to its half-width at half maximum (~1.3 $\rm km\,s^{-1}$). For each species tested, we selected the interval $20<|v|<100$ $\rm km\,s^{-1}$ for the out-of-trail sample, while for the in-trail one we optimized the width. We observed in any case a low dependence of the final significance on the width of the in-trail sample. The error-bars on the two samples were calculated as the square root of the number of data points in each bin (Fig. C.1). This test gives a confidence of 8.1σ, 4.4σ and 5.1σ for Fe I, Fe II, and Cr I, respectively, that the in-trail and out-of-trail distributions are drawn from different parent distributions in night 1. The distributions are compatible with

Table 3. Results of the cross-correlation with theoretical models. ND stands for no detection.

Element	night 1			night 2			combined
	K_p [km s^{-1}]	ΔV_{sys} [km s^{-1}]	S/N	K_p [km s^{-1}]	ΔV_{sys} [km s^{-1}]	S/N	S/N
Fe I	176^{+5}_{-7}	2^{+3}_{-2}	5.3	177^{+3}_{-3}	0^{+1}_{-1}	7.0	7.6
Fe II	163^{+4}_{-3}	-2^{+2}_{-2}	4.1	ND	ND	ND	3.8
Cr I	164^{+7}_{-5}	-1^{+2}_{-3}	3.5	ND	ND	ND	3.1

Table 4. Significance of the detections in night 1 calculated with different statistical methods.

Element	S/N	T-test	KS	bootstrap
Fe I	5.3	8.1σ	6.4σ	6.8σ
Fe II	4.1	4.4σ	3.1σ	4.5σ
Cr I	3.5	5.1σ	4.4σ	3.6σ

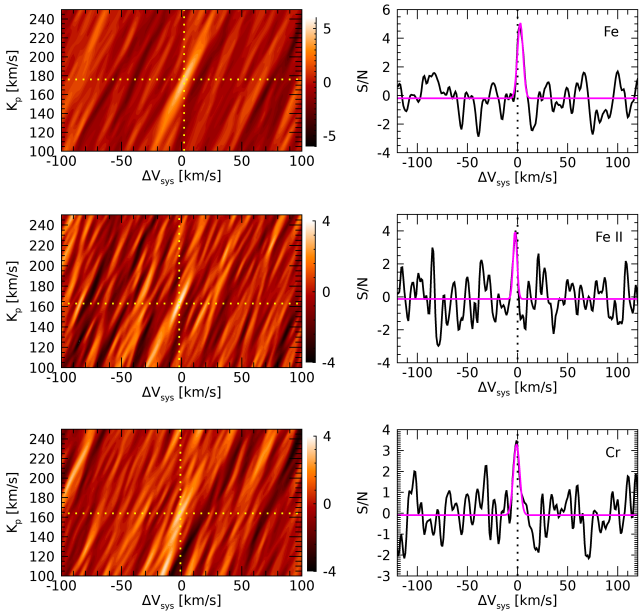

Fig. 4. From top to bottom, detections of Fe I, Fe II, and Cr I in night 1. Left panels show the K_p-ΔV_{sys} maps, with the colour scale in S/N. The yellow dotted lines represent the best signal position. Right panels show the signal at the best K_p position, with a Gaussian fit shown in magenta.

Gaussian functions, calculated by assuming the average of the samples and their standard deviation as the center and the width of the Gaussian, respectively (Fig. C.1), thus validating the use of this statistics. We note however that Cabot et al. (2019) suggest that the Welch t-test could sometimes overestimate the confidence of detections. We thus made also Kolmogorov-Smirnov (KS) statistics on the same distributions, obtaining a confidence of 6.4σ, 3.1σ and 4.4σ for Fe I, Fe II, and Cr I, respectively, that the distributions in- and out-of-trail are different (Table 4).

We did a further statistic significance test by performing a bootstrap, adapting the method proposed in appendix C.2 of Hoeijmakers et al. (2020) to our dataset, where there is no transit. For each species we shifted each cross-correlation function of the time-series to a random radial velocity taken from a uniform distribution, masking all the zones where the planetary signal is expected, and averaged these CCFs. We then fitted a Gaussian profile with a fixed width of 5, 10 or 20 km s^{-1}, centered at a random position in the averaged CCF. This was repeated 100,000 times for each species. In Fig. C.2 we show the resulting distributions coming from random fluctuations for night 1, together with the contrast of the detections, which are significantly stronger. We fitted a Gaussian function to each of the random distributions, took the maximum width σ of the three (which is always the one created with a fixed width of 5 km s^{-1}), and estimated the significance of detection by taking the ratio between the amplitude of the signal and σ (Table 4).

We confirm the detections of Fe I, Fe II and Cr I in night 1 with all the statistical methods used.

5. Discussion and conclusions

Our result confirms the tendency of a temperature inversion in the atmosphere of UHJ caused by absorption of UV and optical stellar light by metals. KELT-20b is the fourth UHJ for which day-side neutral iron emission is detected with high-resolution spectroscopy. All these planets orbit A-type stars. Lothringer & Barman (2019) theoretically showed that the slope of the T-P and the temperature range across the temperature inversion in UHJs both increase as the host star effective temperature increases. It is thus probably not a casualty that all the detections of temperature inversion with high-resolution spectroscopy up to now are for UHJs orbiting A-type stars. These stars have strong UV emission, which is the wavelength range where the metals causing temperature inversions present the largest number of lines (Fossati et al. 2021).

We added Cr I to the species discovered in emission from the dayside of an exoplanet, by performing a multi-species atomic detection of planetary emission. We note that we detected Fe II and Cr I only after occultation, while we see Fe I better before the occultation. In principle, the S/N is almost the same for both nights, so this could hint to different atmospheric properties in the atmosphere at sight during the different orbital phases. An offset in thermal phase curves has been often observed for short-period exoplanets (e.g., Deming & Knutson 2020, and references therein), so one possibility is that the temperature is higher in the atmosphere in view after the occultation, making neutral iron to become more ionized and chrome emission visible. The emission at different planetary phases could be used to constrain the atmospheric dynamics of the planet (e.g. Arcangeli et al. 2021), but an in-depth analysis of different planetary phases however requires a framework of analysis that includes 3D atmospheric modeling. To verify the real atmospheric origin of the differences found, it will be useful to collect more data with high S/N to check the repeatability of the behaviour and possibly constrain the T-P profile directly from the observations.

This work demonstrates that high-resolution emission spectroscopy can be exploited much like high-resolution transmis-

sion spectroscopy for multiple-species detection in exoplanetary atmospheres, allowing us to deeply investigate their three-dimensional characteristics.

Acknowledgements. We acknowledge the support by INAF/Frontiera through the "Progetti Premiali" funding scheme of the Italian Ministry of Education, University, and Research and from PRIN INAF 2019.

References

Arcangeli, J., Désert, J.-M., Line, M. R., et al. 2018, ApJ, 855, L30
Arcangeli, J., Désert, J.-M., Parmentier, V., et al. 2021, A&A, 646, A94.
Baxter C., Désert J.-M., Parmentier V., et al., 2020, A&A, 639, A36.
Bell, T. J. & Cowan, N. B. 2018, ApJ, 857, L20
Birkby, J. L., de Kok, R. J., Brogi, M., et al. 2017, AJ, 153, 138
Borsa, F., Scandariato, G., Rainer, M., et al. 2015, A&A, 578, A64
Borsa, F., Rainer, M., Bonomo, A. S., et al. 2019, A&A, 631, A34
Borsa, F., Allart, R., Casasayas-Barris, N., et al. 2021, A&A, 645, A24
Brogi, M., Giacobbe, P., Guilluy, G., et al. 2018, A&A, 615, A16
Cabot, S. H. C., Madhusudhan, N., Hawker, G. A., et al. 2019, MNRAS, 482, 4422.
Casasayas-Barris, N., Pallé, E., Yan, F., et al. 2018, A&A, 616, A151
Casasayas-Barris, N., Pallé, E., Yan, F., et al. 2019, A&A, 628, A9
Claudi, R., Benatti, S., Carleo, I., et al. 2017, European Physical Journal Plus, 132, 364
Cosentino, R., Lovis, C., Pepe, F., et al. 2014, Proc. SPIE, 9147, 91478C
Deming, D. & Knutson, H. A. 2020, Nature Astronomy, 4, 453
Ehrenreich, D., Lovis, C., Allart, R., et al. 2020, Nature, 580, 597
Fortney, J. J., Lodders, K., Marley, M. S., et al. 2008, ApJ, 678, 1419
Fossati, L., Shulyak, D., Sreejith, A. G., et al. 2020, A&A, 643, A131
Fossati, L., Young, M. E., Shulyak, D., et al. 2021, A&A, 653, A52
Giacobbe, P., Brogi, M., Gandhi, S., et al. 2021, Nature, 592, 205
Gibson, N. P., Merritt, S., Nugroho, S. K., et al. 2020, MNRAS, 493, 2215
Guilluy, G., Sozzetti, A., Brogi, M., et al. 2019, A&A, 625, A107
Guilluy, G., Andretta, V., Borsa, F., et al. 2020, A&A, 639, A49
Hoeijmakers, H. J., Ehrenreich, D., Kitzmann, D., et al. 2019, A&A, 627, A165
Hoeijmakers, H. J., Cabot, S. H. C., Zhao, L., et al. 2020, A&A, 641, A120
Hoeijmakers, H. J., Seidel, J. V., Pino, L., et al. 2020, A&A, 641, A123.
Hubeny, I., Burrows, A., & Sudarsky, D. 2003, ApJ, 594, 1011
Kasper, D. H., Bean, J. L., Line, M. R., et al. 2021, arXiv:2108.08389
Kesseli, A. Y., Snellen, I. A. G., Alonso-Floriano, F. J., et al. 2020, AJ, 160, 228
Lothringer, J. D., Barman, T., & Koskinen, T. 2018, ApJ, 866, 27
Lothringer, J. D. & Barman, T. 2019, ApJ, 876, 69
Lund, M. B., Rodriguez, J. E., Zhou, G., et al. 2017, AJ, 154, 194
Mollière, P., Wardenier, J. P., van Boekel, R., et al. 2019, A&A, 627, A67
Nugroho, S. K., Kawahara, H., Masuda, K., et al. 2017, AJ, 154, 221
Nugroho, S. K., Gibson, N. P., de Mooij, E. J. W., et al. 2020, ApJ, 898, L31
Nugroho, S. K., Gibson, N. P., de Mooij, E. J. W., et al. 2020, MNRAS, 496, 504
Parmentier, V., Line, M. R., Bean, J. L., et al. 2018, A&A, 617, A110
Pino, L., Désert, J.-M., Brogi, M., et al. 2020, ApJ, 894, L27
Rainer, M., Borsa, F., Pino, L., et al. 2021, A&A, A&A, 649, A29
Scandariato, G., Borsa, F., Sicilia, D., et al. 2021, A&A, 646, A159
Snellen, I. A. G., Albrecht, S., de Mooij, E. J. W., & Le Poole, R. S. 2008, A&A, 487, 357
Stangret, M., Casasayas-Barris, N., Pallé, E., et al. 2020, A&A, 638, A26
Talens, G. J. J., Justesen, A. B., Albrecht, S., et al. 2018, A&A, 612, A57
Vidal-Madjar, A., Arnold, L., Ehrenreich, D., et al. 2010, A&A, 523, A57
Yan, F., Pallé, E., Reiners, A., et al. 2020, A&A, 640, L5

Appendix A: Parameters

Table A.1. Physical and orbital parameters of the KELT-20 system used in this work.

Parameter	Value	Reference
	Stellar Parameters	
$T_{\rm eff}$	8980^{+90}_{-130} K	1
$v \sin i$	116.23 ± 1.25 km s^{-1}	2
$M_\star$	$1.89^{+0.06}_{-0.05}$ $M_\odot$	1
$R_\star$	1.60 ± 0.06 $R_\odot$	1
	Planetary parameters	
$M_{\rm p}$	< 3.51 $M_{\rm Jup}$	3
$R_{\rm p}$	1.83 ± 0.07 $R_{\rm Jup}$	1
$T_{\rm eq}$	2260 ± 50 K	1
	Orbital parameters	
T_0	$7909.5906^{+0.0003}_{-0.0002}$ BJD-2450000	1
P	$3.474119^{+0.000005}_{-0.000006}$ days	1
e	0	fixed
$K_{\rm s}$	322.51^* m s^{-1}	4
$K_{\rm p}$	175^* km s^{-1}	
$V_{\rm sys}$	-24.48 ± 0.04 km s^{-1}	2

*Assuming the upper mass limit for the planet.

References. [1] Talens et al. (2018); [2] Rainer et al. (2021); [3] Lund et al. (2017); [4] Casasayas-Barris et al. (2019)

Appendix B: Models

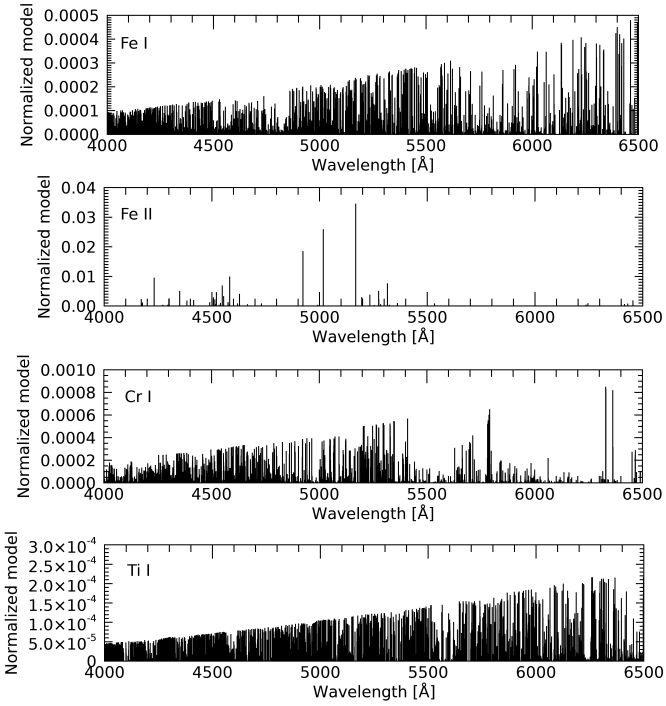

Fig. B.1. From top to bottom, the models of Fe I, Fe II, Cr I and Ti I used for the cross-correlations. The models are normalised to unity.

Appendix C: Statistics

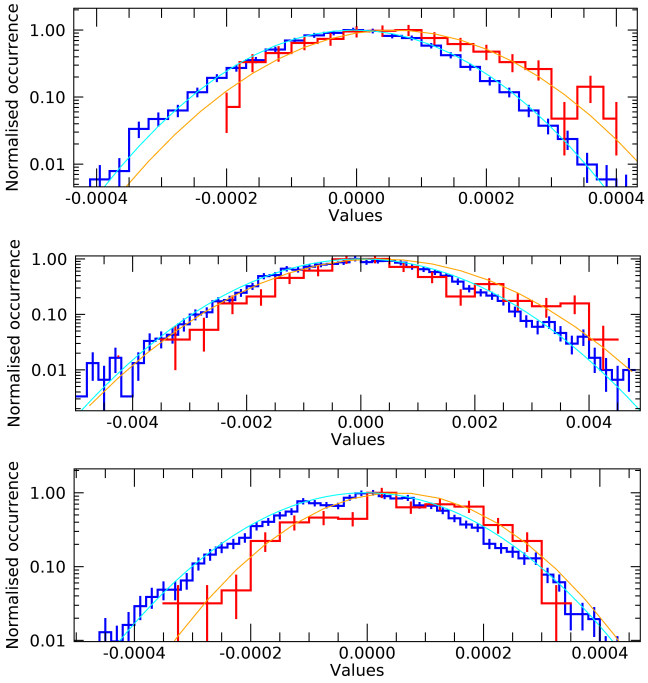

Fig. C.1. Distribution of the night 1 in-trail and out-of-trail samples for Fe I, Fe II, and Cr I, respectively. The blue histogram represents the out-of-trail distribution, while the red histogram the in-trail one. The respective Gaussian distributions are shown as cyan and orange lines.

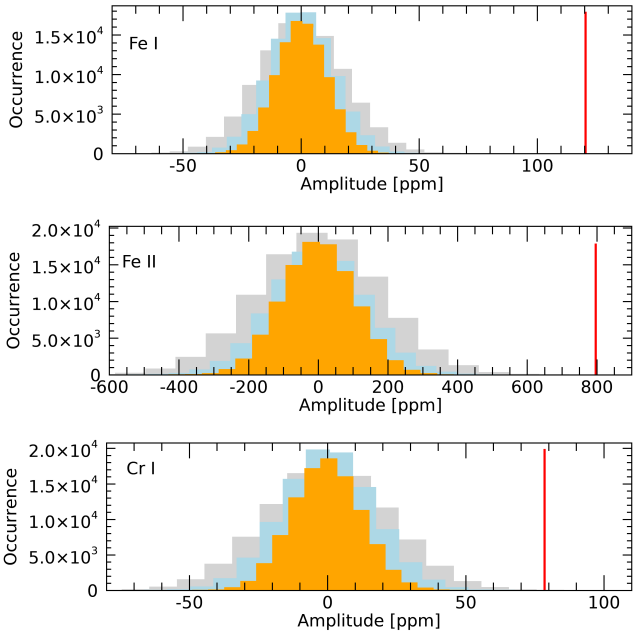

Fig. C.2. Distributions created with the bootstrap method for Fe I, Fe II, and Cr I, respectively. The gray, light blue and orange distributions are coming from fixed widths of 5, 10 and 20 km s^{-1}, respectively. The vertical red lines show the amplitude of the detection.